Eng. Sci., 2025, **36**, 1666

Engineered Science

DOI: https://dx.doi.org/10.30919/es1666

Heteroepitaxial Barium Titanate/Niobium Potassium Oxide Polyimide Nanocomposite Films for High Temperature Energy Storage

Lingke Zhu,[1] Baiqi Jing,[1] Xuyuan Kou,[1] Peimei Yuan,[2] Yifan Li,[3] LinCheng Li,[1] Ben Bin Xu,[3] Ilwoo Seok[4,*] and Dengwei Hu[1,*]

Abstract

Advanced electronic device components demand capacitors with high temperature resistance, high energy storage, and rapid charge and discharge speeds. The utilization of inorganic ceramics and organic polymer nanocomposite films in the field of high temperature energy storage holds the potential to attain this objective. Nevertheless, the primary challenge lies in the susceptibility of the composite film to breakdown under high temperature conditions. In this study, a barium titanate ($BaTiO_3$, BT)/niobium potassium oxide ($KNbO_3$, KN) complex with heteroepitaxial interfaces was prepared via the solvothermal method. Subsequently, BT/KN was filled in the polymerized polyimide (PI). Significantly, at the interface of BT and KN, *p-n* junction is formed. This unique structure effectively restricts the formation of conductive paths, and thereby significantly increases the breakdown field strength and energy density of the composite films. At 25 °C and 150 °C, 5 wt% BT/KN/PI nanocomposite films attained energy densities of 5.45 J/cm^3 and 4.69 J/cm^3, corresponding to the breakdown field strength of 659.84 MV/m and 404.39 MV/m, respectively. Moreover, at 200°C, 3 wt% BT/KN/PI nanocomposite films exhibited an energy storage density of 2.18 J/cm^3 at a breakdown field strength of 224.75 MV/m. This study demonstrates the significant potential of BT/KN/PI nanocomposite film capacitors for high temperature energy storage applications.

Keywords: Energy storage capacitor; High temperature energy storage; High breakdown field strength; Heterostructure.

Received: 29 March 2025; Revised: 24 April 2025; Accepted: 04 May 2025

Article type: Research article.

1. Introduction

Dielectric capacitors represent a significant portion of the capacitor market, constituting approximately 50% of the global market share for capacitors utilized in energy storage devices.[1] Dielectric capacitors are widely utilized in electronic equipment and power supply system because of their rapid charge and discharge rates, as well as their high-power density.[2,3] It has an irreplaceable role in aerospace, hybrid vehicles, and wind power generation.[4-6] However, dielectric capacitors frequently encounter harsh environment of high power, high current, and ultra-high temperatures in practical applications.[7-9] For example, in the aerospace field and in underground oil and gas exploration, temperatures have even exceeded 250 °C.[10,11] The typical solution is to incorporate an external cooling system, but this not only enlarges the size of the capacitor but also raises the operational costs. In addition, the most representative commercial polymer dielectric energy storage material biaxial oriented polypropylene (BOPP), cannot exceed a maximum temperature of 85 °C during long-term use. High-temperature environments can lead to a significant increase in the conduction loss of BOPP, which largely limits its application in the field of high-temperature energy storage.[12-16] Therefore, it is essential to develop dielectric film capacitors with small volume, high temperature resistance, and possess superior energy storage capabilities.

As we all know, the energy storage density (U_e) is given by the equation $U_e = \int E_b\, dD$, where $D = (1/2)\ \varepsilon_0\varepsilon_r$. In this equation, E_b is the breakdown field strength, D is the electric displacement, ε_o is the dielectric constant of vacuum, and ε_r is the relative dielectric constant. Additionally, U_e can also be expressed as $1/2\ \varepsilon_0\varepsilon_r E_b^2$.[17-19] According to the formula above, the energy storage density of a dielectric capacitor is related to both the electric field strength and the dielectric constant, and these two factors are positively correlated. The dielectric constant is negatively correlated with electric field strength; therefore, it is crucial to balance the relationship between the

---

[1] *Key Laboratory of Functional Materials of Baoji, Baoji University of Arts and Sciences, 1 Hi-Tech Avenue, Baoji, Shaanxi, 721013, China*

[2] *Northwestern Polytechnical University and Shaanxi Joint Laboratory of Graphene, School of Materials Science and Engineering, State Key Laboratory of Solidification Processing, Center for Nano Energy Materials, Xi'an, Shaanxi, 710072, China*

dielectric constant and electric field strength.[20,21] The organic polymer film offers several advantages, including excellent flexibility, lightweight properties, and ease of processing. In recent years, organic polymers such as polyimide (PI),[22,24] polyetherimide (PEI),[25,26] fluorinated polyimide (FPI),[27,28] polyester (PET),[29,30] and polycarbonate (PC)[31,32] have garnered significant attention due to their high glass transition temperatures (T_g). Additionally, the E_b of polymer electrolyte energy storage materials can exceed an order of magnitude higher than traditional materials. However, this performance is often hindered by a low dielectric constant and a limited polarization value, which restricts the enhancement of its U_e value to a certain extent. Incorporating inorganic ceramic fillers with high dielectric constants is one of the most effective strategies to address this issue.[33,34] Consequently, the development of organic/inorganic nanocomposite energy storage materials has become increasingly popular among researchers. Nevertheless, the introduction of inorganic ceramic fillers frequently results in a reduction of breakdown field strength and an increase in leakage conductivity due to challenges related to agglomeration or uneven dispersion. Employing insulating fillers or constructing carrier traps presents a viable solution to these challenges.[35]

The two-dimensional (2D) fillers such as titanate[36,37] and niobate,[38] can enhance the breakdown field strength due to their excellent insulating properties and large aspect ratio, by limiting the transport of charge carriers and disperse the growth path of electrical branches.[39,40] Researchers previously applied barium titanate (BT) nanoparticles and 2D hexagonal boron nitride nanosheets (BNN) into a P(VDF-CTFE) matrix, to achieve high energy density of 21.2 J/cm^3 at a breakdown field strength of 552 MV/m.[41] The high permittivity of PVDF and the strongly polar C-F bond in its molecular structure also enhance charge storage capacity under high electric fields. Moreover, the introducing of two materials with distinct band structures, can generate heterojunctions upon their combination. Therefore, an internal electric field can be generated at the interface, creating a high energy barrier that effectively inhibits charge carrier transport across the interface. Su *et al.*, incorporate 0.3 ZrO_2@$KNbO_3$(KN) with a heterogeneous structure into FPI matrix to obtain a U_e of 7.9 J /cm^3 at 150 °C, with a breakdown field strength of 550 MV/ m.[27] In addition to the influence of energy barrier, FPI optimizes the molecular structure by introducing F atoms, improves the dielectric constant, and significantly improves the energy storage density.

In this study, we developed a series of high-temperature-resistant inorganic/organic nanocomposite films with varying quantities of inorganic fillers. Initially, the BT/KN complex with a heteroepitaxial interface was synthesized using a solvent-thermal method, resulting in the formation of a *p-n* heterojunction at the interface. The internal electric field generated by this heterojunction significantly enhanced the separation of charge carriers while inhibiting charge transport. Additionally, the zero-dimensional (0D) and 2D insulating fillers effectively obstructed the propagation of breakdown paths and dispersed the breakdown of electrical branches. The synthesized BT/KN was incorporated into PI matrix, which contributed to a higher glass transition temperature. The results indicate that the breakdown field strength and energy density of the BT/KN/PI nanocomposite films are significantly improved through the synergistic effects of the inorganic and organic components. At room temperature, E_b increased to 659.84 MV/m, and U_e reached 5.45 J/cm^3. More importantly, at elevated temperatures of 150°C and 200°C, E_b and U_e also achieved values of 404.39 MV/m and 224.75 MV/m, and 4.69 J/cm^3 and 2.18 J/cm^3, respectively. This work presents a novel strategy for enhancing the energy storage performance of inorganic/organic nanocomposite thin films at high temperatures.

2. Results and discussion

Fig. 1a and b show the preparation process of BT/KN filler and BT/KN/PI nanocomposite film. Fig. 1c mainly describes the significance of this work and the mechanism of performance improvement. The high breakdown field strength of BT/KN/PI nanocomposite film is firstly because the two-dimensional sheet structure of BT/KN has a large specific surface area, which can effectively prevent electrical breakdown. The 2D sheet materials embedded in a polymer matrix create numerous interface regions, enhancing interactions between polymer molecules and molecular chains. These structures introduce deep trap levels that can capture free charge carriers and inhibit their transfer, acting as an effective barrier to charge movement. Consequently, this makes it challenging to establish a conductive path within the material, thereby reducing conduction losses and space charge accumulation—two primary factors contributing to electric field distortion. In addition, the lamellar structure can facilitate an even distribution of the electric field in the in-plane direction, thereby preventing local electric field concentration. When 2D fillers are arranged in parallel within the matrix, the discharge path can be extended along the surface of the fillers, significantly lengthening the breakdown path, and delaying breakdown. Furthermore, when lamellar KN and granular BT are combined and incorporated into the PI matrix as fillers, they can also cover a limited number of holes and cracks in the film matrix, thereby reducing electric field concentration at lattice parameters. When these two materials are combined, a lattice mismatch phenomenon occurs, leading to the formation of a heteroepitaxial interface. defects. These mechanisms work synergistically to enhance the breakdown field strength of the composite. Second, *n*-type semiconductor BT and *p*-

---

[3]*Department of Mechanical and Construction Engineering, Faculty of Engineering and Environment, Northumbria University, Newcastle Upon Tyne, NE18, UK*

[4]*College of Engineering and Computer Science, Arkansas State University, Jonesboro, Arkansas, 72467, USA*

**Email*: iseok@astate.edu (I. Seok); dwhu@bjwlxy.edu.cn (D. Hu)

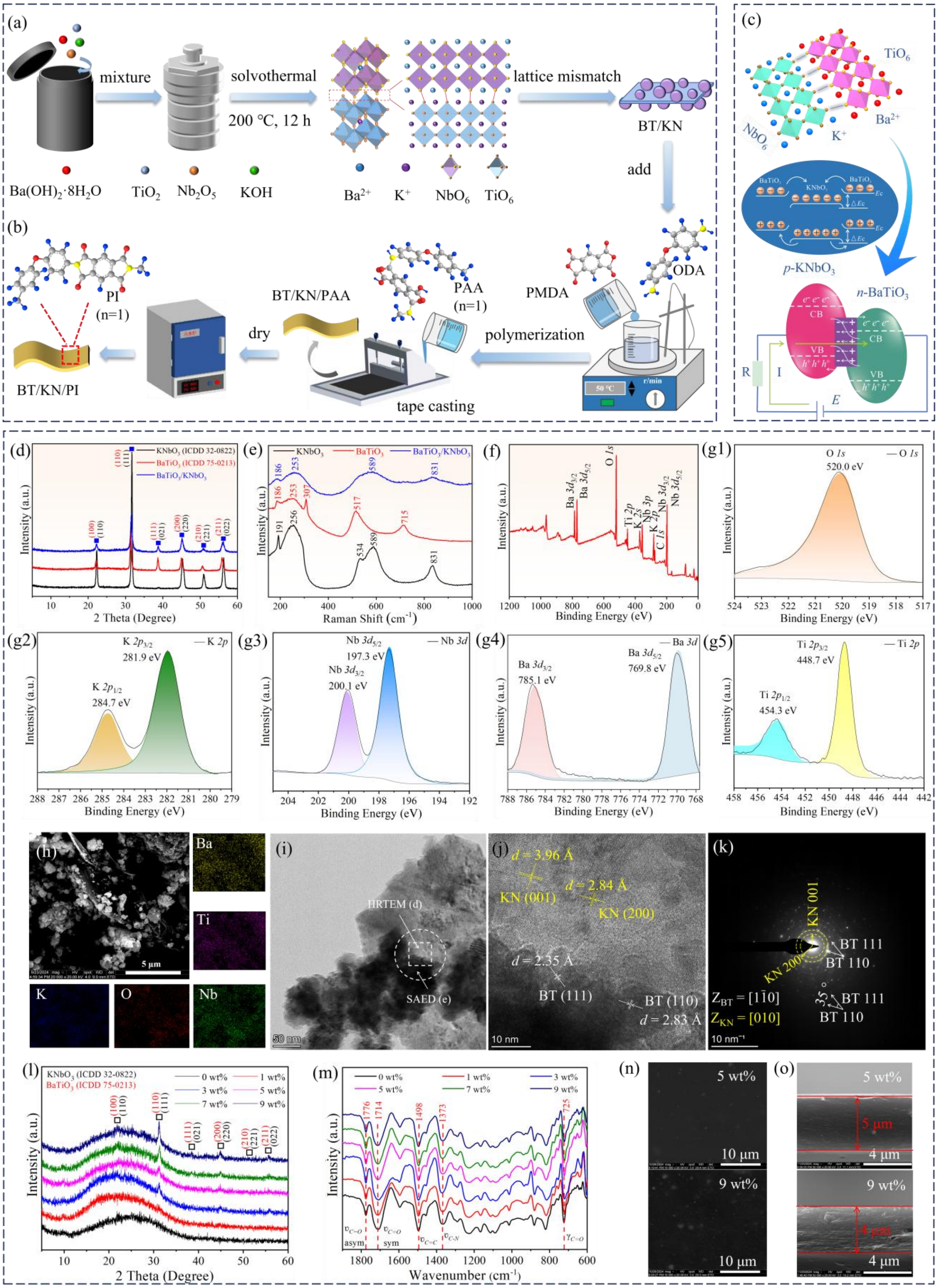

Fig. 1: Preparation process of (a) BT/KN filler, (b) BT/KN nanocomposite film, (c) *p-n* junction diagram, (d) XRD patterns, (e) Raman spectra, (f) XPS full spectrum and (g1-g5) fine spectra of K, Nb, Ba, Ti, O elements of BT/KN, (h) SEM image and Mappings, (i) TEM image, (j) HRTEM image, (k) SAED pattern of BT/KN, (l) XRD patterns, (m) FT-IR spectra of BT/KN/PI nanocomposite films, (n) surface and (o) cross-section of BT/KN/PI nanocomposite films with 5 and 9 wt% fillers, respectively.

type semiconductor KN are two types of perovskite crystals that possess similar yet distinct When the *p*-type semiconductor, which is dominated by holes, encounters the *n*-type semiconductor, which is dominated by electrons, band bending occurs at the interface due to the difference in energy levels between the two materials. Consequently, the electrons and holes from each material will diffuse into the other. The excess holes will migrate to the *n*-region, while the excess electrons will migrate to the *p*-region until equilibrium is achieved. Following the formation of the *p-n* junction, this carrier diffusion process creates a space charge region near the junction, resulting in an internal electric field and establishing a potential barrier at the center of the junction. The internal electric field drives electrons toward the *n*-region and holes toward the *p*-region; however, the barrier and defects at the interface impede their complete separation, causing some carriers to become trapped near the interface. Simultaneously, a potential difference is generated between the two sides of the *p-n* junction, with the *n*-side exhibiting a higher potential and the *p*-side a lower potential. Consequently, the direction of the electric field within the *p-n* junction is from the *n*-type semiconductor to the *p*-type semiconductor. Conversely, the electric field generated by the applied voltage opposes that of the *p-n* junction. This opposition facilitates the separation of external charge carriers and inhibits the formation of conductive paths within the material. The charge redistribution at the heterojunction interface can also create an electric dipole layer, which generates a local electric field that further restricts carrier motion. Consequently, the *p-n* junction can form carrier traps and enhance the energy density of the material through the synergistic effects of band theory, interface engineering, and the built-in electric field.

2.1. Phase, morphology, and structure analysis of BT/KN

XRD results for BT, KN, and BT/KN are shown in Fig. 1d BT and KN correspond to standard cards 75-0213 and 32-0822, respectively, indicating that BT exhibits a cubic phase while KN displays an orthorhombic phase. The XRD diffraction peaks for BT/KN align with the peak positions of both BT and KN. Furthermore, the BT/KN composite reveals crystal faces corresponding to BT, specifically (100), (110), (111), (200), (201), (211) crystal faces corresponding to KN, namely (110), (111), (021), (220), (221), (022). These findings preliminarily confirm the successful preparation of the BT/KN composite. Fig. 1e illustrates the results of the Raman spectrum analysis for BT, KN, and BT/KN. The characteristic peaks for BT are observed at 186, 253, 307, 517, and 715 cm^{-1}, while the characteristic peaks for KN are found at 191, 256, 534, 589, and 831 cm^{-1}. Raman peaks of the BT/KN exhibit characteristic peaks at 186^{-1} and 253 cm^{-1}, corresponding to BT, and at 589^{-1} and 831 cm^{-1}, corresponding to KN. The variations in other peaks may be attributed to two-phase recombination. As shown in Fig. 1f, the full XPS spectrum of BT/KN revealed the presence of K, Nb, Ba, Ti and O elements. This finding, in conjunction with the test results, further supports the successful synthesis of BT/KN. Fig. 1 g1-g5 presents the detailed spectra of the elements. In the fine spectrum of Nb element, the $3d_{3/2}$ and $3d_{5/2}$ orbitals of Nb are observed at the binding energies of 200.1 eV and 197.3 eV, respectively, indicating that the chemical valence state of Nb element is +5 valence. In the fine spectrum of Ti, the $2p_{1/2}$ and $2p_{3/2}$ orbitals of Ti are detected at the binding energies of 454.3 eV and 448.7 eV, respectively, signifying that the chemical valence state of Ti is +4 valence.

The micro-morphologies of BT, KN, and BT/KN were examined using SEM, as illustrated in Fig. S1a and c. The BT sample exhibited a granular structure, while the KN sample displayed a blocky morphology. EDS and mapping analyses also revealed a more uniform distribution of elements (Fig. S1b and d). Notably, in the SEM image of BT/KN (Fig. 1h) reveals the presence of two distinct phases: granular BT and flaky KN. This observation may be attributed to the aggregation of KN when the two phases are combined, which promotes the formation of the flaky structure. It can be observed from the BT/KN EDS and Mapping in Fig. 1h and S2 that the distribution of elements within the complex is relatively uniform. Fig. 1i-k display the test results obtained from the BT/KN TEM, HRTEM, and SAED, respectively. The presence of two distinct phases, two-dimensional flake KN and zero-dimensional granular BT, is evident in the TEM image, and the morphology aligns with the results obtained from SEM. HRTEM revealed lattice fringes with lattice spacing of 2.35Å and 2.83 Å, which can be attributed to the (111) and (110) crystal faces of BT, respectively. Additionally, lattice fringes with lattice spacing of 3.96Å and 2.84Å were identified, corresponding to the (001) and (200) crystal faces of KN. Furthermore, distinct grain boundaries are observable in the BT/KN complex. SAED pattern displays the reciprocallattice points of the BT single crystal aligned along the [110] direction, alongside the diffraction rings of the KN polycrystal with the crystal band axis in the [010] direction. This provided strong evidence for the successful integration of BT and KN.

2.2. Structural characterization of BT/KN/PI nanocomposite films

In the XRD pattern of BT/KN/PI nanocomposite films with varying amounts of BT/KN addition (Fig. 1l), amorphous diffraction peaks are observed at approximately 20°, which is a typical characteristic peak of the polymer PI. When the BT/KN addition is 0 wt%, only a single peak corresponding to PI is present. As the amount of BT/KN increases, the characteristic peaks of BT/KN gradually emerge and intensify. Six crystal face characteristic peaks (100), (110), (111), (200), (201), (211) belonging to BT and six crystal face characteristic peaks (110), (111), (021), (220), (221), (022) belonging to KN can be observed. There were no peaks indicating the presence of other impurities. This shows that the physical composite of BT/KN/PI is of high quality, with no chemical reaction occurring between BT/KN and PI, and that the nanocomposite film has been preliminarily successfully prepared. In the FT-IR spectra of pure PI and BT/KN/PI nanocomposite films (Fig. 1m), symmetric C=O stretching, asymmetric C=O stretching, C-C stretching, C-N stretching, and C-O stretching belonging to the imide group were observed at 1714, 1776, 1498, 1373, and 725 cm^{-1}, respectively. The figure indicates that the C=O vibration peak is strong, suggesting a high degree of imidization and a significant level of polymerization within the polymer. The surface SEM images of BT/KN/PI nanocomposite films with BT/KN additions of 5 wt% and 9 wt% are presented in Fig. 1n. The surface SEM of BT/KN/PI nanocomposite films with varying filler concentrations (0 wt%, 1 wt%, 3 wt%, and 7 wt%) are presented in Fig. S3a-d. The SEM images reveal that the surface of the nanocomposite film is well-prepared, exhibiting no significant holes or pores. At lower BT/KN filling rates, there is no noticeable agglomeration within the nanocomposite film. However, as the BT/KN filling rate increases, slight agglomeration becomes evident on the surface of the nanocomposite film, particularly in the 9 wt% BT/KN/PI nanocomposite film. This agglomeration may be attributed to non-uniform dispersion resulting from the increased filler content. The surface topography of BT/KN/PI flexible nanocomposite films with different amounts of BT/KN was tested by AFM (Fig. S4). It can be seen that the surface of all composite films was relatively flat, and no obvious defects and cracks appeared in the composite films, which was consistent with the structure tested by SEM on the surface. Fig. 1o and S3e-h display the sectional SEM images of BT/KN/PI nanocomposite films with different BT/KN concentrations following cold extraction with liquid nitrogen. The thickness of the pure PI film measures 2 μm, while the thickness of the BT/KN/PI nanocomposite films with varying BT/KN concentrations ranges from approximately 4 to 5 μm, demonstrating relative uniformity. The accumulation of fillers within the composite film can lead to local electric field distortion, thereby diminishing the energy storage performance. The cross-section of the composite film reveals that the packing material is evenly dispersed throughout the film, with no significant agglomeration observed. This uniform distribution is attributed to the use of an alternating ultrasonic stirring method during the polymerization process. EDS and mapping tests were performed on the cross-sections of BT/KN/PI nanocomposite films with varying filler amounts (Fig. S5). The concentrations of Ba, Ti, K, Nb, and O elements in the composite films increased with the addition of BT/KN. The mapping results further illustrate the distribution of each element within the composite film as the BT/KN filler amount increases. Additionally, the findings from XRD and FT-IR tests corroborate each other, providing robust evidence for the successful synthesis of BT/KN/PI nanocomposite films.

2.3. Performance analysis of BT/KN/PI nanocomposite films

The thermal stability of the BT/KN/PI nanocomposite film was evaluated (Fig. 2a), and the results indicated that the composite film exhibited excellent heat resistance and thermal stability. When the thermogravimetric loss rate of all nanocomposite films reached 10%, the T_g was found to be above 508℃. Fig. 2b presents the calculated decomposition temperature and thermal stability index T_{HRI} of the composite film at various heat loss rates. Notably, when the heat loss rates were 5% and 30%, the thermal stability index remained above 225 °C. The results indicate that the BT/KN/PI nanocomposite films, with varying amounts of additives, exhibit excellent thermal stability, a slow thermal decomposition rate, and minimal weight loss. High thermal stability is a crucial factor for the effective performance of composite films in high-temperature environments. The experimental findings demonstrate that the incorporation of BT/KN filler enhances other properties of the composite film without compromising its thermal stability. This conclusion establishes a foundation for the reliable operation of BT/KN/PI nanocomposite films under extreme conditions. The results of the static water contact angle test for nano-composite films with varying amounts of BT/KN additions were statistically analyzed, as shown in Fig. 2c, with specific angle indications provided in Fig. S6. A larger contact angle indicates better hydrophobicity of the material. As illustrated in Fig. 2c, the contact angle of the nano-composite film increases with the amount of BT/KN added, suggesting an enhancement in hydrophobicity. This increase in hydrophobicity effectively prevents the penetration and adsorption of water, allowing the BT/KN/PI nanocomposite film to exhibit waterproof, anti-fouling, and moisture-proof properties in practical applications. Fig. 2d illustrates the ultraviolet absorption spectrum of BT/KN/PI nanocomposite films with varying amounts of additives. All composite films exhibit strong absorption within the wavelength range of 200-500 nm. In comparison to pure PI films, the primary absorption peaks of the BT/KN/PI nanocomposite films are observed around 425 nm, with no significant blue shift detected. This indicates that the addition of BT/KN inorganic ceramic filler does not influence the UV absorption strength of the films. As the amount of BT/KN increases, the UV absorption strength of the composite films initially rises and then declines. When the BT/KN content reaches 3 wt%, the UV absorption intensity reaches the maximum of 0.69. These findings suggest that BT/KN/PI nanocomposite films hold potential application value in the field of novel thin-film ultraviolet sensors. Increasing the band gap of the composite film necessitates more energy for charge carriers to transition from the valence band to the conduction eV. When these materials are combined as inorganic fillers in PI-based energy storage films, the band gap is reduced compared to that of pure PI films (Fig. 2e and S7). However, this reduction does not adversely affect the energy storage band. Under normal conditions, the band gap of BT is approximately 3.4 eV, while the band gap of KN is around 3.3 performance of the composite film, as demonstrated by subsequent analyses. This phenomenon may occur because the

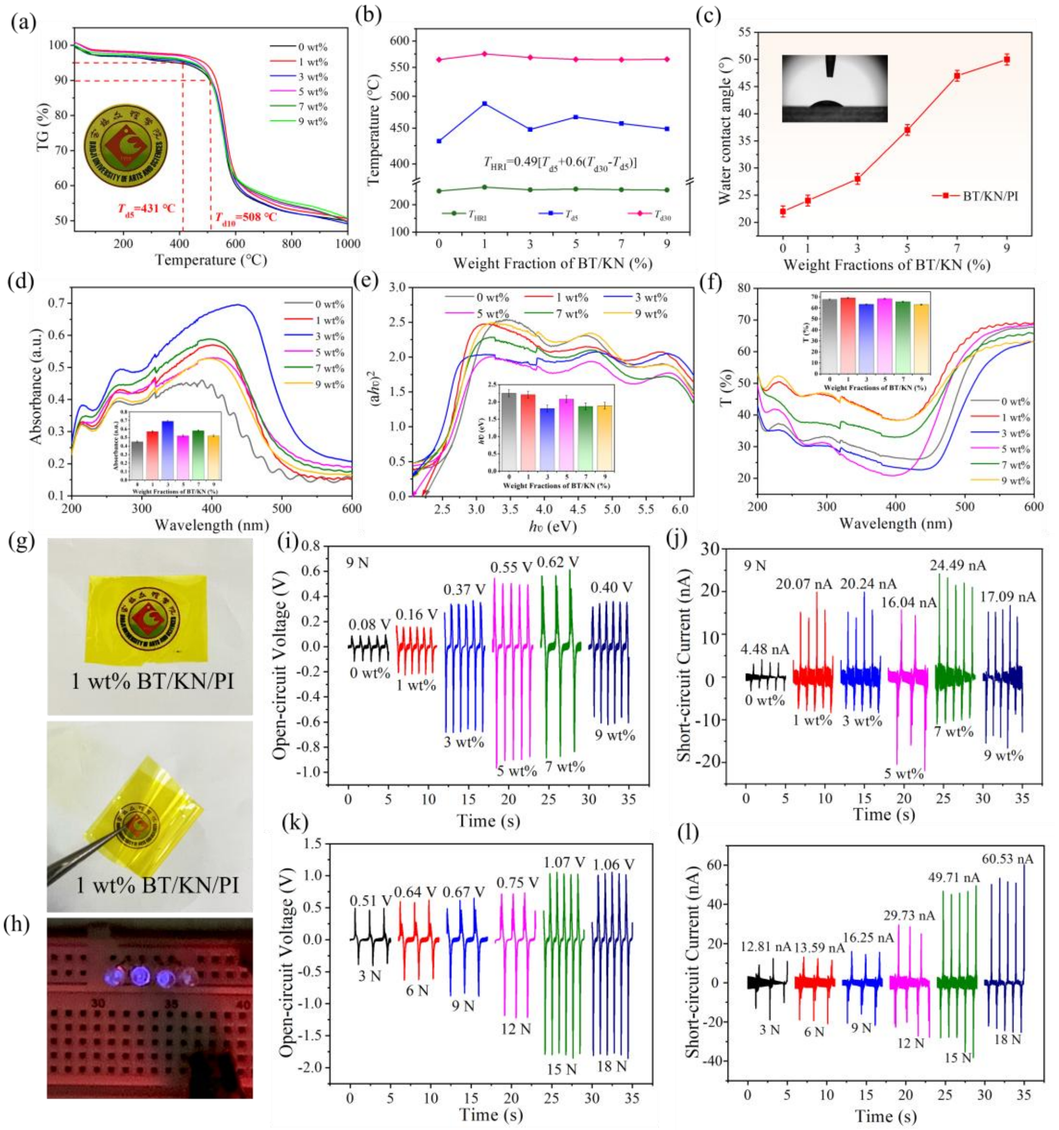

Fig. 2: (a) TG curves, (d) Thermogravimetric data, (c) Contact angle statistics, (d) UV absorption, (e) Band gap width, (f) Transmittance of BT/KN/PI nanocomposite films with different BT/KN filling ratios, (g) 1 wt% BT/KN/FPI nanocomposite films and curvature test of the 1 wt% BT/KN/PI nanocomposite films, (h) A physical image of lighting a small bulb, (i, j) V_{oc} and I_{sc} of BT/KN/PI composite films with different addition amounts under 9 N pressure and (k, l) V_{oc} and I_{sc} of 7 wt% BT/KN/PI composite film under different pressures.

p-n junction formed by the combination of BT and KN facilitates the separation of charge carriers, thereby requiring higher energy to achieve the transition of charge. From the optical images of pure PI films and BT/KN/PI nanocomposite films with varying filler concentrations, it is evident that the overall color of the PI-based films is golden (Fig. S8). However, as the amount of BT/KN filler increases, the transparency of the composite film gradually decreases. The transmittance tests conducted on all films (Fig. 2f) indicate that the transmittance of the BT/KN/PI nanocomposite films shows little variation compared to that of the pure PI films. This suggests that the addition of BT/KN filler does not significantly impact the transparency of the composite film, which retains its transparent appearance. Consequently, BT/KN/PI composites hold promise for various applications in visualization.

BT/KN/PI nanocomposite films have good flexibility (Fig. 2g and S9), which helps to prepare them into sensor parts. BT/KN/PI nanocomposite film can light 3.0-3.2 VF light bulbs through pressure sensing (Fig. 2h, see support information video 1 for specific tests). Fig. S10 shows the principal circuit diagram of BT/KN/PI flexible nanocomposite film lighting small bulb. It can be clearly seen from the figure that the relationship between the small light bulb, the BT/KN/PI composite film, and the applied voltage. The power generation principle of the composite film is further demonstrated. The open circuit voltage (V_{oc}) and short circuit current (I_{sc}) of the composite film were measured by a self-assembled piezoelectric sensing system (see support information video 2 for specific tests). When BT/KN/PI nanocomposite films are subjected to 9 N pressure, the test results of V_{oc} and I_{sc} are shown in Fig. 2i and j. The results

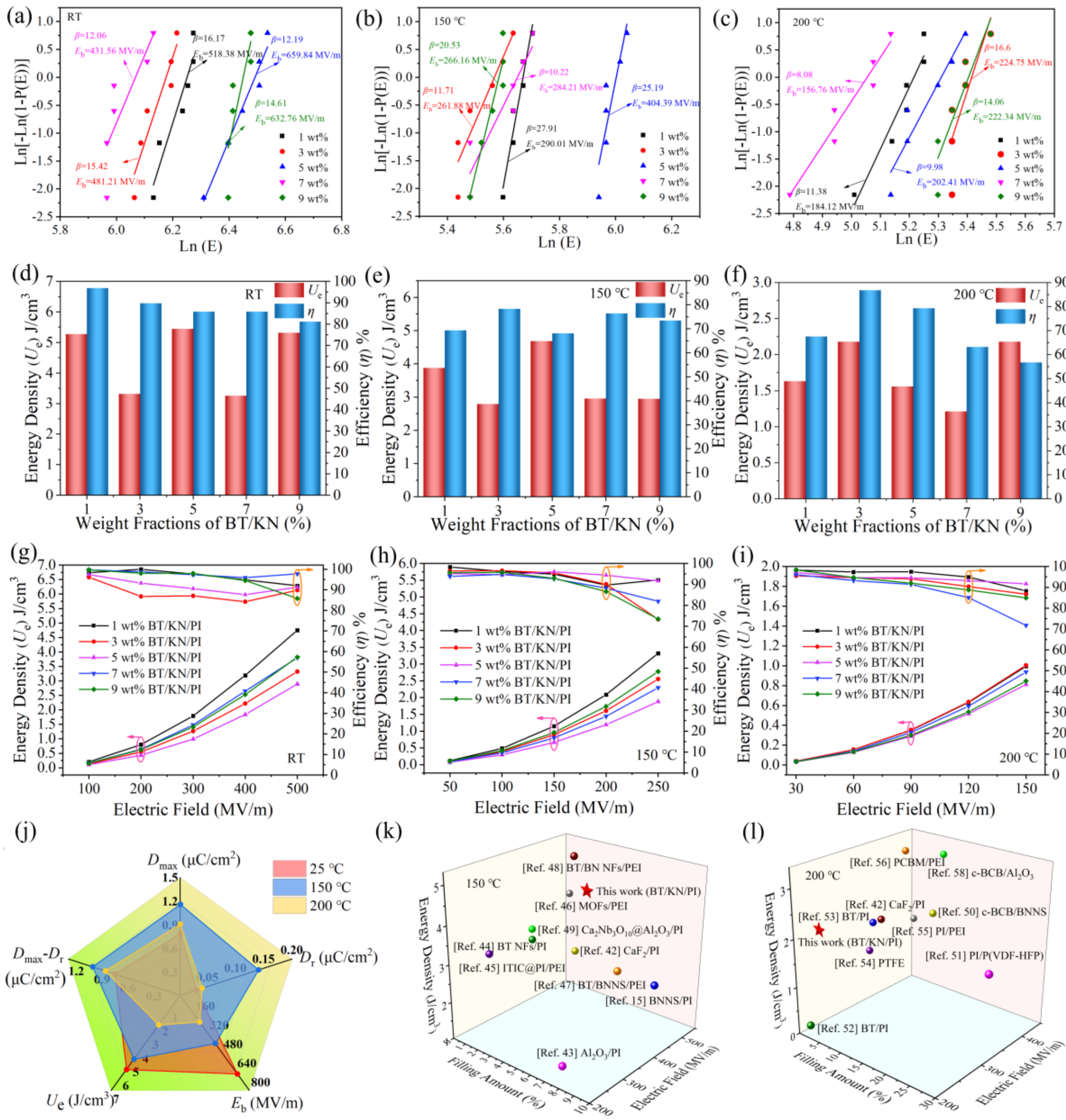

Fig. 3: Statistical diagrams of (a-c) *Weibull* distribution, (d-f) U_e and η statistical graphs, (g-i) U_e and η trends of BT/KN/PI nanocomposite films with different BT/KN filling rates at (a, d, g) room temperature, (b, e, h) 150 °C and (e, f, i) 200 °C, respectively, (j) radar diagram of electrical properties of BT/KN/PI nanocomposite films at room temperature, 150 °C and 200 °C, (k, l) comparison of E_b and U_e of BT/KN/PI nanocomposite films is based on doping works and this work[15][42-56] and this work.

show that the V_{oc} and I_{sc} produced by all composite films are proportional to the load, and the nano-composite films with different BT/KN addition amounts can produce stable piezoelectric output. When the amount of BT/KN is 7 wt%, the V_{oc} is 0.62 V, and the I_{sc} is 24.49 nA. A piezoelectric sensing test was conducted on the 7 wt% BT/KN/PI composite film with an increase of 3 N (Fig. 3k and l) The results showed that V_{oc} and I_{sc} also increased steadily with the increase of applied pressure, indicating that the composite film had stable and good piezoelectric sensing performance. To evaluate the chemical stability of BT/KN/PI nanocomposite films, both pure PI and BT/KN/PI nanocomposite films were immersed in KOH and HCl solutions, each with a concentration of 5 mol/L (Fig. S11). The condition of the nanocomposite films was assessed immediately upon wetting and after soaking for 24, 48, and 72 h. The BT/KN/PI nanocomposite film initially appeared as a flat, golden yellow in the KOH solution. However, after soaking for 24, 48, and 72 h, the film exhibited a fading phenomenon, resulting in a light-yellow color and curling. Notably, the composite film did not dissolve, melt, or degrade in the strong alkaline solution. Additionally, the condition of all films in the HCl solution was monitored. After soaking for 24, 48, and 72 h, the films maintained the same appearance as when they were first immersed, remaining flat and golden yellow without significant changes. In summary, the BT/KN/PI nanocomposite film demonstrates excellent chemical stability, allowing it to withstand strong acidic and alkaline environments without dissolving. This characteristic significantly broadens the potential applications of BT/KN/PI nanocomposite films.

The energy storage performance of BT/KN/PI nanocomposite films with varying amounts of BT/KN was evaluated using a ferroelectric test system at room temperature, 150 ℃, and 200℃, respectively. *Weibull* distribution statistics (Fig. 3a-c) were conducted for the three sets of test results, and the intrinsic breakdown field strength and shape factor β (Fig. S12) of all composite films were calculated. At room temperature, the shape factor β for all the composite films exceeded 10, indicating that the prepared composite films exhibit relatively high stability. When the BT/KN content is 5 wt%, the maximum intrinsic breakdown field strength reaches 659.84 MV/m. At an elevated temperature of 150 ℃, the intrinsic breakdown field strength of the BT/KN/PI nanocomposite film with a 5 wt% addition can achieve 404.39 MV/m. Furthermore, the β value for all BT/KN/PI nanocomposite films remained above 10. As the temperature increases to 200 ℃, the β value for most of the BT/KN/PI nanocomposite films also exceeds 10, which indicates that the composite films maintain good stability under these high-temperature conditions. The maximum breakdown field strength of 224.75 MV/m was achieved with a 3 wt% addition of BT/KN. Test results under various temperature conditions indicate that at low BT/KN filling levels, such as in a 1 wt% BT/KN/PI nanocomposite film, the breakdown field strength does not significantly increase. This is likely because the inorganic fillers do not form an orderly and uniform arrangement at low filling levels, which may result in direct breakdown of the composite film as the applied voltage increases. Furthermore, when the BT/KN filler content is increased to 7 wt%, the breakdown field strength of the composite film decreases significantly. This reduction may be attributed to high-voltage breakdown caused by the agglomeration of the filler particles.

When energy density is expressed in U_e and energy loss is expressed in U_{loss}, $\eta = U_e/(U_e+U_{loss})$. The integrated area between the upper half of the hysteresis loop and the Y-axis in the *D-E* loop curve can be expressed as U_e, and the area enclosed within the hysteresis loop can be expressed as U_{loss}. Both the increase of U_e and the decrease of U_{loss} can effectively enhance the η value of the composite film. The *D-E* loops curves of BT/KN/PI nanocomposite films at room temperature, 150℃ and 200℃ were drawn (Fig. S13), and energy storage density U_e and the charge and discharge efficiency η at intrinsic breakdown field strength were calculated. Fig. 3d-f shows the statistics of the energy density and efficiency of all composite films. When the test condition is set to room temperature, the *D-E* loop curve of the BT/KN/PI nanocomposite film exhibits a relatively narrow shape. This indicates that the energy loss of the composite film under these conditions is minimal, suggesting that the leakage current is also low. When the concentration of BT/KN was 5 wt%, U_e reached a maximum of 5.45 J/cm^3, η could attain 85.88%. However, when the temperature was increased to 150 ℃, the *D-E* loop curve displayed a "fat" phenomenon compared to the test results obtained at room temperature. This phenomenon can be attributed to the distortion of the electric field within the composite film under high temperature and high electric field conditions. As a result, numerous positive and negative charges accumulate near the filler, potentially forming a localized region of high conductivity. This accumulation leads to an increase in high-temperature leakage conductance, resulting in elevated U_{loss}. However, since the *p-n* junction still inhibits the formation of conductive pathways for charge carriers, U_e of the 5 wt% BT/KN/PI nanocomposite films can still reach 4.69 J/cm^3, with an η of 68.1% at 150 ℃. As the temperature increases to 200 ℃, the leakage conduction phenomenon becomes more pronounced, resulting in a sharp decrease in both U_e and E_b. At this temperature, the U_e of the 5 wt% BT/KN/PI nanocomposite film drops to 1.56 J/cm^3. Conversely, when the BT/KN content is reduced to 3 wt%, the U_e of the composite film increases to 2.18 J/cm^3. This finding surpasses the results of most relevant studies conducted to date. In addition, the maximum electrical displacement (D_{max}), minimum electrical displacement (D_r), the difference between D_{max} and D_r (D_{max}-D_r), and E_b of composite films are closely related to U_e. Fig. S14 illustrates D_{max}, D_r, and D_{max}-D_r of BT/KN/PI nanocomposite films at various test temperatures. Under the testing conditions of room temperature and 150 ℃, the D_{max} of 5 wt% BT/KN/PI nanocomposite films can reach 0.79 μC/cm^2 and 1.16 μC/cm^2, respectively, while D_{max}-D_r is 0.76 and 1.02 μC/cm^2, which is higher than that of most other filled composite films. At a temperature of 200 ℃, the D_{max} of the 3 wt% BT/KN/PI nanocomposite film can reach 0.91 μC/cm^2, with a maximum D_{max}-D_r of 0.87 μC/cm^2. This discussion indicates that by incorporating an appropriate amount of BT/KN inorganic ceramic filler, the polarization value of nanocomposite films can be significantly enhanced, thereby providing favorable conditions for achieving a high energy storage density in composite films.

The same applied voltage was continuously increased under consistent temperature test conditions, and U_e and η of BT/KN/PI nanocomposite films were statistically measured (Fig. 3g-i). As the applied voltage increased, the energy storage density of all BT/KN/PI nanocomposite films exhibited an overall upward trend, regardless of whether the temperature was at room temperature, 150℃, or 200℃. This trend can be attributed to the fact that as the applied voltage increases, the E_b of the composite film also rises, leading to an increase in D_{max}. In a high-temperature environment of 200 ℃, the electric field intensity of 150 MV/m results in a U_e of 1.01 J/cm^3 for the 3 wt% BT/KN/PI nanocomposite film. However, as the breakdown field strength increases, the charge and discharge efficiency decrease because of the high electric field. Additionally, the leakage current of BT/KN/PI nanocomposite films rises at temperatures of 150 ℃ and 200 ℃. This increase is attributed to local electric field distortion caused by the combination of high temperature and high electric field, which exacerbates high-temperature leakage conductance. Consequently, compared to BT/KN/PI nanocomposite films at room temperature, η decreases with rising temperature. However, at 150 °C and 250 MV/m, as well as at 200 °C and 150 MV/m, the η of all composite films remained above 70%. Fig. 3j presents the statistical results of the energy storage performance of BT/KN/PI nanocomposite films under the test conditions of room temperature, 150 °C, and 200 °C, respectively, illustrating the dependence of the composite films on temperature. A comparison of the findings from this study with those from related fields reveals, as shown in Fig. 3k, that the E_b and U_e of BT/KN/PI nanocomposite films at 150 °C outperform the energy storage performance of most polymer-based nanocomposite films reported to date. At 200 °C, their performance remains at a mid to upper level (Fig. 3l).

In summary, the analysis of the energy storage performance of BT/KN/PI nanocomposite films with varying additive amounts reveals that these composite films exhibit relatively high energy density, particularly under elevated temperature conditions of 150 °C and 200 °C. This performance can be primarily attributed to the selection of the PI matrix. The molecular chain bond energy of PI is high, and its thermal decomposition temperature typically exceeds 500 °C, significantly surpassing that of conventional polymers. The glass transition temperature of PI generally ranges from 300 °C to 400 °C, and it also possesses a high breakdown field strength (> 300 kV/mm) at elevated temperatures. However, the permittivity of PI is relatively low (approximately 3.0 to 3.5), and since permittivity is directly proportional to energy density, this presents a limitation. To address this, BT and KN, both of which have high permittivity, are introduced in this study. These materials are incorporated into the PI matrix as fillers, significantly enhancing the overall permittivity. Additionally, the introduction of BT and KN creates a lattice mismatch, resulting in the formation of a *p-n* heterojunction at the heteroepitaxy interface. The internal electric field of the heterostructure opposes the applied electric field, and an energy barrier is established between the BT and KN semiconductors, effectively trapping charge carriers and inhibiting their transport. Furthermore, the parallel arrangement of 2D morphology of the fillers contributes to an increase in breakdown field strength. The synergistic effects of these mechanisms substantially enhance the energy density and efficiency of BT/KN/PI nanocomposite films at high temperatures.

To analyze the effects of temperature, breakdown field strength E_b, D_{max}, D_r, and D_{max}-D_r on U_e and η of BT/KN/PI nanocomposite films more intuitively, the same applied voltage is maintained across each temperature condition. The hysteresis loops are statistically represented as *D-E* loops. Fig. 4a-e illustrate the *D-E* loops of BT/KN/PI nanocomposite films at 200 °C under varying breakdown field strengths. The inner mosaic diagram presents statistics for D_{max} and D_r at different breakdown field strengths. At a test temperature of 200 °C, when the breakdown field strength is 150 MV/m, the D_{max} of the 3 wt% BT/KN/PI nanocomposite film reaches 0.67 μC/cm^2, while the difference D_{max}-D_r attains a maximum of 0.64 μC/cm^2 (Fig. 4f). This observation is consistent with the U_e results of the 3 wt% BT/KN/PI nanocomposite films mentioned above. All BT/KN/PI nanocomposite films exhibit an increase in the breakdown field strength. The *D-E* loop curves of all BT/KN/PI nanocomposite films, obtained at room temperature and 150 °C (Fig. S15 and S16), also adhere to this trend. Furthermore, as the test temperature increases, the electro-hysteresis loop of the composite film at elevated temperatures appears significantly more `obese` compared to the conditions observed at room temperature. At room temperature, the electro-hysteresis loop of the film material is the narrowest, while the composite film tested at 150°C is also narrower than that tested at 200 °C. The conclusion that the internal area of the hysteresis loop increases under high temperature and high electric field conditions is based on the observation that, under these influences, electric field distortion occurs within the BT/KN/PI composite, leading to the formation of a localized high conductivity region. At this point, a significant accumulation of positive and negative charges occurs near the BT/KN filler, which facilitates the formation of a conductive path along the direction of the applied electric field between adjacent BT/KN fillers, thereby exacerbating the leakage conductance phenomenon.

The multi-physics coupling finite element analysis of BT/KN/PI nanocomposite films with varying amounts of BT/KN addition was conducted. At a breakdown field strength of 450 MV/m, the potential distribution diagrams for all BT/KN/PI nanocomposite films (Fig. S17) were initially simulated, revealing a relatively uniform surface potential distribution across all composite films. Fig. S18 illustrates the longitudinal section potential diagrams of BT/KN/PI nanocomposite films with different amounts of addition. At low BT/KN filling levels, the potential distribution remains relatively uniform; however, as the BT/KN content increases, localized polarization phenomena become evident within the film. This phenomenon may be attributed to the increase in the BT/KN content, which alters the local charge density within the film, leading to an uneven distribution of the electric field. Additionally, the lower surface of the composite film was grounded, while a field strength of 450 MV/m was applied to the upper surface. Fig. 4g-i and S19 illustrate the simulated electrical breakdown path of the BT/KN/PI nanocomposite film. When the BT/KN content is 1 wt% or 3 wt%, the filling amount is relatively low, and the 2D flake morphology does not significantly enhance the dispersion of electric branches. Consequently, the electric branches are prone to directly breaking down from the PI matrix, resulting in poor breakdown resistance of the BT/KN/PI nanocomposite films. When the addition of BT/KN reaches 5 wt%, the filling amount is moderate, and the appropriate quantities of 2D flake and 0D granular fillers are evenly distributed within the PI matrix. This distribution effectively blocks and disperses the breakdown paths of the electrical branches, thereby improving the breakdown field strength. The energy density of BT/KN/PI

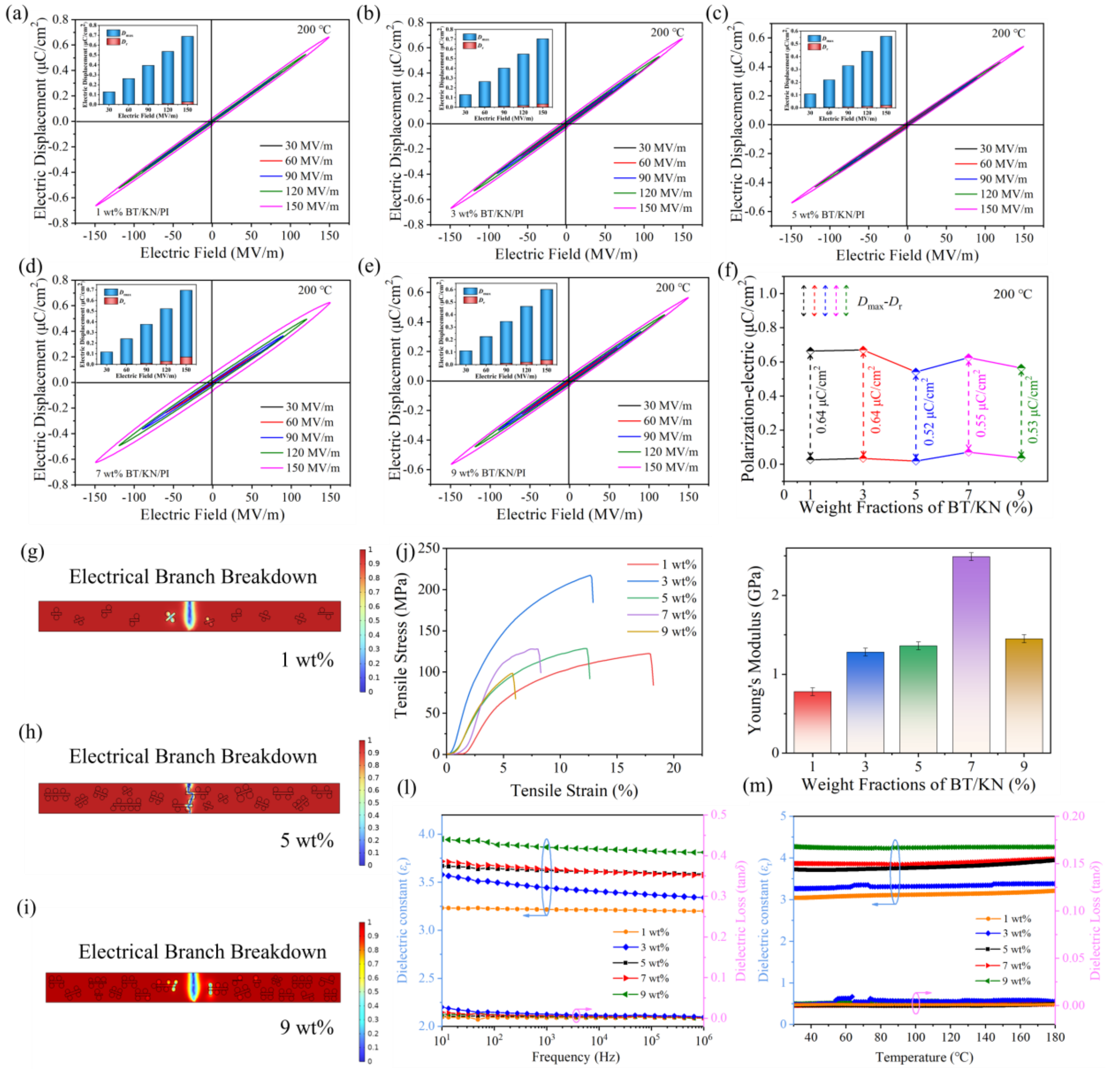

Fig. 4: BT/KN/PI nanocomposite films with varying BT/KN filling rates at 200 °C (a-e) D-E loops at different E_b and (f) D_{max}, D_r, D_{max}-D_r at150 MV/m, (g-i) Breakdown path simulation diagrams of 1 wt%, 5 wt% and 9 wt% BT/KN/PI nanocomposite films with different BT/KN addition amounts, (j) stress-strain curves, (k) Young's modulus, (l) Frequency spectrum and (m) dielectric temperature spectra of BT/KN/PI nanocomposite films with different BT/KN filling rates.

nanocomposite films was simulated (Fig. S20), and the results obtained were consistent with the experimental findings. The simulation results align with the actual test outcomes. However, when the volume of the BT/KN filler increased to 7 wt% and 9 wt%, a direct breakdown phenomenon in the electrical branches was observed. This can be attributed to the increased filler content, which led to agglomeration or interface effects of BT/KN. A significant accumulation of charges near the filler, combined with the external electric field, formed a conductive path, resulting in a reduction of the breakdown field strength. The energy density of the 5 wt% BT/KN/PI nanocomposite film reaches its maximum, as confirmed by the simulation of electrical branch breakdown.

The stress-strain curves of BT/KN/PI nanocomposite flims with varying amounts of BT/KN additions were evaluated using a multipurpose testing machine (Fig. 4j). Notably, the shape variable for all BT/KN/PI nanocomposite films remained low (< 0.2), indicating a high rigidity of the composite films. Fig. 4k illustrates the Young's modulus of the BT/KN/PI nanocomposite films. It is evident that as the amount of BT/KN filler increases, the Young's modulus of the composite film initially rises and then subsequently decreases. When a material exhibits a high Young's modulus, it can effectively reduce stress concentration and local deformation due to a more uniform internal stress distribution. Energy storage films typically need to maintain stability over multiple cycles during actual use. Consequently, an improvement in Young's modulus enhances the composite film's resistance to deformation, allowing it to retain a stable shape when subjected to external forces. The Young's modulus of the 7 wt% BT/KN/PI nanocomposite film reaches a maximum of 2.49 GPa, indicating that the BT/KN/PI nanocomposite film possesses high rigidity and durability. As shown in Fig. 4l, the dielectric constant (ε_r) of the BT/KN/PI nanocomposite film remained relatively stable across the test frequency range of 10-10^6 Hz. The dielectric constant of the composite film gradually increased with the addition of BT/KN filler. However, ε_r decreased under higher frequency test conditions. This decline may be attributed to the inability of interfacial polarization and space charge polarization at the two-phase interface to keep pace with the rapid changes in the applied high-frequency electric field. Additionally, the short depolarization time of the dipoles contributes to the corresponding decrease in ε_r of the composite film. The dielectric loss (tan δ) of the BT/KN/PI nanocomposite film remains low (< 0.05) across the frequency spectrum, from low to high frequency.[57] The dielectric properties of BT/KN/PI nanocomposite films were investigated over a temperature range of 30 to 180 °C at a frequency of 10^6 Hz (Fig. 4m). The ε_r of all BT/KN/PI nanocomposite films remained basically stable throughout the tested temperature range, while tan δ exhibited a slight increase with rising temperature. However, the overall level of tan δ remained low. These results indicate that the BT/KN/PI nanocomposite films can maintain stable performance across a wide temperature range.

3. Conclusion

In this study, we successfully prepared a BT/KN complex composed of 2D flakes and 0D particles with a heteroepitaxial interface using the solvothermal method. This complex was then incorporated into PI matrix to create BT/KN/PI nanocomposite films. On one hand, the 2D sheet fillers possess a larger specific surface area, which enhances their resistance to breakdown. On the other hand, the combination of the BT and KN phases results in the formation of a *p-n* junction at the heteroepitaxial interface, which effectively promotes the separation of charge carriers. The opposing directions of the internal and external electric fields create a carrier trap, limiting the transport of charge carriers and inhibiting the formation of conductive pathways within the film, thereby reducing the likelihood of breakdown avalanches. Notably, the 5 wt% BT/KN/PI nanocomposite film achieves U_e of 4.69 J/cm^3 and an η of 68.1% at E_b of 404.39 MV/m when tested at a temperature of 150 °C. Even at the elevated temperature of 200 °C, the 3 wt% BT/KN/PI nanocomposite film can reach U_e of 2.18 J/cm^3 at a maximum E_b of 224.75 MV/m. This work provides an effective mechanism for enhancing the energy storage performance of polyimide-based flexible energy storage materials at high temperatures.

4. Experimental section

Materials: Niobium oxide (Nb_2O_5, 99.9%, AR), barium hydroxide octahydrate ($Ba(OH)_2{\cdot}8H_2O$, 98%, AR), 4,4'-oxybisbenzenamine ether (ODA, 98%), pyromellitic dianhydride (PMDA, 99%), isopropyl alcohol (C_3H_8O, ≥99.5%, AR), and N,N-Dimethylacetamide (DMAc, ≥99.8%) were purchased from Shanghai Maclin Biochemical Co., Ltd. Titanium dioxide (TiO_2, 99.8%, AR) was obtained from Tianjin Kemiou Chemical Reagent Co., Ltd. Potassium hydroxide (KOH, 90%, AR) was sourced from Chengdu Aikeda Chemical Reagent Co., Ltd. Anhydrous ethanol (CH_3CH_2OH, 99.5%, AR) and acetic acid (CH_3COOH, 99.8%, AR) were acquired from the China Pharmaceutical Reagent Network. All chemicals and reagents were used as received.

Sample Preparation: The preparation process of BT/KN with a heteroepitaxial interface is illustrated in Fig. 1a. TiO_2, $Ba(OH)_2{\cdot}8H_2O$ (0.13 mol/L), Nb_2O_5, and KOH (2.1 mol/L) were placed in a Teflon-lined reactor (50 mL), and isopropyl alcohol (25 mL) was added as the solvent. The stirred solution was placed on a magnetic agitator for 1 h and then transferred to the homogeneous reactor for solvothermal reaction at 200°C for 12 h. After cooling to room temperature, the products were alternately washed several times with deionized water, acetic acid (5%), and ethanol. The resulting products were dried in a drying oven at 60 °C for 12 h to obtain BT/KN with a heteroepitaxial interface. Fig. 1b primarily outlines the process of preparing BT/KN/PI nanocomposite films through in-situ polymerization. In this study, 4,4'-diaminodiphenyl ether (ODA) and phthalic anhydride (PMDA) were selected as monomers, and the ratio of ODA to PMDA set at 1:1.05. Prior to the experiment, the two monomers were dried in a vacuum drying oven at 80 °C for 12 h to eliminate moisture. First, six parts of ODA were weighed, dissolved in a specific amount of DMAc solvent, and stirred for 30 min to obtain an ODA-DMAc mixed solution. Next, six parts of PMDA were weighed, and varying amounts of the BT/KN complex were measured according to the desired quantities of inorganic fillers. This mixture was then added to PMDA and dissolved in DMAc, stirring for an additional 30 min to produce the BT/KN-PMDA-DMAc mixed solution. The two solutions were thoroughly mixed, and the ODA-DMAc solution was uniformly transferred to the BT/KN-PMDA-DMAc solution five times over the course of one hour. Subsequently, under the conditions of a 0 °C ice water bath, ultrasonic stirring was alternated for 24 h to obtain a viscous BT/KN/PAA slurry, which was then placed in a vacuum drying oven for 30 min to remove bubbles. The composite film was prepared using the casting method, with the BT/KN/PAA slurry poured onto a glass substrate measuring 13 cm*13 cm. The paste was applied evenly with a scraper, and the thickness of the film was controlled by adjusting the height of the scraper. The film was dried in a vacuum oven at 60 °C for 12 h to remove the solvent, and was subsequently transferred to a muffle furnace for heat treatment. The material was heated at 100 °C, 200 °C and 300 °C respectively for 1 h each, resulting in the complete transformation of PAA into PI. After naturally cooling to room temperature, the film was removed from the furnace and soaked in deionized water. After stripping, a BT/KN/PI flexible nanocomposite film was obtained.

Characterizations: The crystal structures of the BT/KN complex and BT/KN/PI nanocomposite films were analyzed using an X-ray diffractometer (XRD, UltimaIV). The micromorphology of BT/KN, as well as the surface and cross-sectional morphology of the BT/KN/PI nanocomposite films, was examined using field emission scanning electron microscopy (SEM, Quanta FEG 250G). The crystal structure of BT/KN was analyzed by field emission transmission electron microscopy (TEM, Talos F200i). The structure and characteristic vibration peaks of the BT/KN and BT/KN/PI nanocomposite films were assessed using a laser Raman spectrometer (inVia) and a Fourier infrared spectrometer (FT-IR, aixACCT). The chemical bonds, binding energy, and element composition of BT/KN were analyzed using X-ray photoelectron spectroscopy (XPS, AXIS ULTRADLD). The thermal stability of the BT/KN/PI nanocomposite films was evaluated with a synchronous thermal analyzer (STA 449F3, Neutsch GMBH) at a temperature range from room temperature to 1000 °C. The hydrophobic properties of different composite films were measured using a contact angle measuring instrument (HITACHI, Japan). The absorption, transmittance, and band gap of the different BT/KN/PI nanocomposite films were determined using a solid-state ultraviolet near-infrared spectrometer (UV-Vis, PerkinElmer). The stress-strain curves and Young's modulus of the film samples were measured using a universal testing machine (RTEC, MYF-3000, USA). The dielectric temperature spectrum and the spectrum of the nanocomposite films were analyzed using a dielectric tester (Novo control concept 80, Germany). The temperature range for this test was from room temperature to 200 °C, and the frequency range was 10^2-10^6 Hz. The piezoelectric sensing properties of the composite films were tested using a homemade piezoelectric testing system that performs periodic reciprocating motion at constant frequency and pressure. The energy storage performance of the BT/KN/PI nanocomposite film at both room temperature and elevated temperatures was tested using a ferroelectric test system (TF2000, German aixACCT Company), a test frequency was 100 Hz.

Multi-physics coupling finite element simulation: The three-dimensional (3D) potential distribution, energy density, cross-section potential, and electrical branch breakdown path of BT/KN/PI nanocomposite films with varying additive amounts were calculated and plotted using the COMSOL system.

Acknowledgements

This work was supported in part by the National Natural Science Foundation of China (No. 52472116, No. 21005003), the Natural Science Basic Research Plan in Shaanxi Province of China (2019JM-091), the Industrial Science and Technology Plan in Shaanxi Province of China (22JC004), the Graduate Innovative Research Project of Baoji University of Arts and Sciences (YJSCX23ZD07), the Graduate Innovative Research Project of Baoji University of Arts and Sciences (YJSCX24ZD07).

Conflict of Interest

The authors declare no conflict of interest.

Supporting Information

Supporting Information is available from the Wiley Online Library or the author.

CRediT Statement

Lingke Zhu: Writing – review & editing, Writing – original draft, Supervision, Methodology, Investigation, Formal analysis, Data curation, Conceptualization. **Baiqi Jing:** Methodology, Investigation, Conceptualization. **Xuyuan Kou:** Software, Resources, Investigation. **Peimei Yuan:** Resources, Investigation. **Yifan Li:** Supervision, Investigation. **Lincheng Li:** Resources, Investigation, Formal analysis. **Ben Bin Xu:** Supervision. **Ilwoo Seok:** Writing – review & editing, Supervision. **Dengwei Hu:** Writing – review & editing, Supervision, Resources, Funding acquisition, Formal analysis.

References

[1] H. Li, Y. Zhou, Y. Liu, L. Li, Y. Liu, Q. Wang, Dielectric polymers for high-temperature capacitive energy storage, *Chemical Society Reviews*, 2021, **50**, 6369-6400, doi: 10.1039/D0CS00765J.

[2] H. Palneedi, M. Peddigari, G.-T. Hwang, D.-Y. Jeong, J. Ryu, High-performance dielectric ceramic films for energy storage capacitors: progress and outlook, *Advanced Functional Materials*, 2018, **28**, 1803665, doi: 10.1002/adfm.201803665.

[3] J.-W. Zha, M. Xiao, B. Wan, X. Wang, Z.-M. Dang, G. Chen, Polymer dielectrics for high-temperature energy storage: Constructing carrier traps, *Progress in Materials Science*, 2023, **140**, 101208, doi: 10.1016/j.pmatsci.2023.101208.

[4] T. Zeng, L. Meng, L. Cheng, R. Wang, Z. Ran, D. Liu, J. Fu, J. He, Q. Zhou, Q. Li, Q. Li, C. Yuan, Scalable hybrid films of polyimide-animated quantum dots for high-temperature capacitive energy storage utilizing quantum confinement effect, *Advanced Functional Materials*, 2025, **35**, 2419278, doi: 10.1002/adfm.202419278.

[5] P. Yuan, R. Xue, Y. Wang, Y. Su, B. Zhao, C. Wu, W. An, W. Zhao, R. Ma, D. Hu, Horizontally-oriented barium titanate@polydomine/polyimide nanocomposite films for high-temperature energy storage, *Journal of Colloid and Interface Science*, 2024, **662**, 1052-1062, doi: 10.1016/j.jcis.2024.02.109.

[6] J.-W. Zha, Y. Tian, M.-S. Zheng, B. Wan, X. Yang, G. Chen, High-temperature energy storage polyimide dielectric materials: polymer multiple-structure design, *Materials Today Energy*, 2023, **31**, 101217, doi: 10.1016/j.mtener.2022.101217.

[7] X. Lin, M. Salari, L. M. R. Arava, P. M. Ajayan, M. W. Grinstaff, High temperature electrical energy storage: advances, challenges, and frontiers, *Chemical Society Reviews*, 2016, **45**, 5848-5887, doi: 10.1039/c6cs00012f.

[8] J. Mao, S. Wang, L. Zhang, Y. Chen, Y. Cheng, Flexible epoxy film: Moderate crosslinking enhances the high temperature energy storage performance, *International Journal of Energy Research*, 2020, **44**, 7580-7590, doi: 10.1002/er.5489.

[9] Z. Ren, L. Lei, L. Zhu, S. Xia, R. Fan, D. Dastan, H. Cui, Z. Shi, Remarkably boosted high-temperature electrostatic energy storage of polyetherimide film induced by TiO_2@Au@AlO_x@Au core-shell nanofibers, *Advanced Functional Materials*, 2025, **35**, 2417156, doi: 10.1002/adfm.202417156.

[10] M. Yang, S. Wang, J. Fu, Y. Zhu, J. Liang, S. Cheng, S. Hu, J. Hu, J. He, Q. Li, Quantum size effect to induce colossal high-temperature energy storage density and efficiency in polymer/inorganic cluster composites, *Advanced Materials*, 2023, **35**, 2301936, doi: 10.1002/adma.202301936.

[11] Q. Li, F.-Z. Yao, Y. Liu, G. Zhang, H. Wang, Q. Wang, High-temperature dielectric materials for electrical energy storage, *Annual Review of Materials Research*, 2018, **48**, 219-243, doi: 10.1146/annurev-matsci-070317-124435.

[12] K. Zhang, Z. Ma, Q. Fu, H. Deng, Multi-layered boron nitride/polyimide high-temperature capacitor dielectric film, *Materials Today Energy*, 2022, **29**, 101093, doi: 10.1016/j.mtener.2022.101093.

[13] S. Ding, Z. Bao, Y. Wang, Z. Dai, J. Jia, S. Shen, Y. Yin, X. Li, Excellent high-temperature dielectric energy storage of flexible all-organic polyetherimide/poly(arylene ether urea) polymer blend films, *Journal of Power Sources*, 2023, **570**, 233053, doi: 10.1016/j.jpowsour.2023.233053.

[14] X. Xu, W. Liu, Y. Li, Y. Wang, Q. Yuan, J. Chen, R. Ma, F. Xiang, H. Wang, Flexible mica films for high-temperature energy storage, *Journal of Materiomics*, 2018, **4**, 173-178, doi: 10.1016/j.jmat.2018.04.003.

[15] K. Zhang, Z. Ma, H. Deng, Q. Fu, Improving high-temperature energy storage performance of PI dielectric capacitor films through boron nitride interlayer, *Advanced Composites and Hybrid Materials*, 2022, **5**, 238-249, doi: 10.1007/s42114-021-00329-7.

[16] Z. Wang, M. Li, B. Liu, G. Yang, M. Luo, T. Zhang, L. Li, Y. Cheng, Z. Jia, G. Wu, Enhanced energy storage characteristics of the epoxy film with rigid phenyl-flexible etherified methylene chains, *Journal of Materials Science & Technology*, 2024, **183**, 12-22, doi: 10.1016/j.jmst.2023.10.026.

[17] L. Sun, F. Zhang, L. Li, J. Liang, J. Dong, Z. Pan, Y. Niu, J. Chen, Y. Liu, Y. Lu, K. Wu, Q. Li, J. Li, Q. Wang, H. Wang, Superior capacitive energy storage enabled by molecularly interpenetrating interfaces in layered polymers, *Advanced Materials*, 2025, **37**, 2412561, doi: 10.1002/adma.202412561.

[18] Z. Wang, T. Wang, M. Fang, C. Wang, Y. Xiao, Y. Pu, Enhancement of dielectric and electrical properties in BFN/Ni/PVDF three-phase composites, *Composites Science and Technology*, 2017, **146**, 139-146, doi: 10.1016/j.compscitech.2017.04.023.

[19] C. Zhang, X. Zhang, B. Zhang, C. Yin, Y. Zhang, Y. Zhang, T. Zhang, Y. Cui, Q. Chi, High-energy storage performance achieved in PbZrO3 thin films *via* Li^+ doping and low-temperature annealing, *Thin Solid Films*, 2024, **794**, 140289, doi: 10.1016/j.tsf.2024.140289.

[20] Z. Pan, S. Xing, H. Jiang, J. Liu, S. Huang, J. Zhai, Highly enhanced discharged energy density of polymer nanocomposites *via* a novel hybrid structure as fillers, *Journal of Materials Chemistry A*, 2019, **7**, 15347-15355, doi: 10.1039/c9ta03292d.

[21] X. Zhang, B.-W. Li, L. Dong, H. Liu, W. Chen, Y. Shen, C.-W. Nan, Superior energy storage performances of polymer nanocomposites *via* modification of filler/polymer interfaces, *Advanced Materials Interfaces*, 2018, **5**, 1800096, doi: 10.1002/admi.201800096.

[22] L. Zhu, Z. Zheng, W. Xu, Y. Tang, H. Yao, Y. Zhang, Z. Jiang, Optimizing high-temperature capacitive energy storage performance by constructing crosslinked structure in self-crosslinkable polyetherimides, *Materials Today Energy*, 2022, **30**, 101145, doi: 10.1016/j.mtener.2022.101145.

[23] P. Ma, C. Dai, H. Wang, Z. Li, H. Liu, W. Li, C. Yang, A review on high temperature resistant polyimide films: Heterocyclic structures and nanocomposites, *Composites Communications*, 2019, **16**, 84-93, doi:

10.1016/j.coco.2019.08.011.

[24] H. Li, M. R. Gadinski, Y. Huang, L. Ren, Y. Zhou, D. Ai, Z. Han, B. Yao, Q. Wang, Crosslinked fluoropolymers exhibiting superior high-temperature energy density and charge–discharge efficiency, *Energy & Environmental Science*, 2020, **13**, 1279-1286, doi: 10.1039/C9EE03603B.

[25] C. Zhang, X. Tong, T. Zhang, Y. Zhang, Y. Zhang, X. Zhang, C. Tang, Q. Chi, Constructing a dual gradient structure of energy level gradient and concentration gradient to significantly improve the high-temperature energy storage performance of all organic composite dielectrics, *Chemical Engineering Journal*, 2024, **491**, 151634, doi: 10.1016/j.cej.2024.151634.

[26] Y. Zhang, Y. Guo, Y. Liu, Z. Shi, W. Liu, J. Su, G. Chen, D. Zhou, All-organic ArPTU/PEI composite dielectric films with high-temperature resistance and high energy-storage density, *Journal of Materials Chemistry C*, 2024, **12**, 4426-4432, doi: 10.1039/D3TC04715F.

[27] Y. Su, Y. Jia, D. Hu, S. Zhu, X. Yang, X. Che, Y. Gong, Y. Fan, W. Wang, H. Fan, Fluorinated Polyimides incorporated with heterogeneous ZrO_2@$KNbO_3$ as multiple carrier transport barriers for Ultra-High energy storage, *Chemical Engineering Journal*, 2024, **500**, 157559, doi: 10.1016/j.cej.2024.157559.

[28] W. Ren, M. Yang, L. Zhou, Y. Fan, S. He, J. Pan, T. Tang, Y. Xiao, C.-W. Nan, Y. Shen, Scalable ultrathin all-organic polymer dielectric films for high-temperature capacitive energy storage, *Advanced Materials*, 2022, **34**, e2207421, doi: 10.1002/adma.202207421.

[29] T. Ju, X. Chen, D. Langhe, M. Ponting, E. Baer, L. Zhu, Enhancing breakdown strength and lifetime of multilayer dielectric films by using high temperature polycarbonate skin layers, *Energy Storage Materials*, 2022, **45**, 494-503, doi: 10.1016/j.ensm.2021.12.009.

[30] Y. Cui, Y. Feng, T. Zhang, C. Zhang, Q. Chi, Y. Zhang, X. Wang, Q. Chen, Q. Lei, Excellent energy storage performance of ferroconcrete-like all-organic linear/ferroelectric polymer films utilizing interface engineering, *ACS Applied Materials & Interfaces*, 2020, **12**, 56424-56434, doi: 10.1021/acsami.0c16197.

[31] F. Guo, X. Shen, J. Zhou, D. Liu, Q. Zheng, J. Yang, B. Jia, A. K. T. Lau, J.-K. Kim, Highly thermally conductive dielectric nanocomposites with synergistic alignments of graphene and boron nitride nanosheets, *Advanced Functional Materials*, 2020, **30**, 1910826, doi: 10.1002/adfm.201910826.

[32] X. Wu, X. Chen, Q. M. Zhang, D. Q. Tan, Advanced dielectric polymers for energy storage, *Energy Storage Materials*, 2022, **44**, 29-47, doi: 10.1016/j.ensm.2021.10.010.

[33] B. Luo, Z. Shen, Z. Cai, E. Tian, Y. Yao, B. Li, A. Kuršumović, J. MacManus-Driscoll, L.-T. Li, L.-Q. Chen, X.-H. Wang, Layered nanosheets: superhierarchical inorganic/organic nanocomposites exhibiting simultaneous ultrahigh dielectric energy density and high efficiency (adv. funct. mater. 8/2021), *Advanced Functional Materials*, 2015, **31**, 2170050, doi: 10.1002/ADFM.202170050.

[34] T. Wang, R.-C. Peng, W. Peng, G. Dong, C. Zhou, S. Yang, Z. Zhou, M. Liu, 2–2 type PVDF-based composites interlayered by epitaxial (111)-oriented BTO films for high energy storage density, *Advanced Functional Materials*, 2022, **32**, 2108496, doi: 10.1002/adfm.202108496.

[35] T. Zhang, H. Sun, C. Yin, Y. H. Jung, S. Min, Y. Zhang, C. Zhang, Q. Chen, K. J. Lee, Q. Chi, Recent progress in polymer dielectric energy storage: From film fabrication and modification to capacitor performance and application, *Progress in Materials Science*, 2023, **140**, 101207, doi: 10.1016/j.pmatsci.2023.101207

[36] F. Wen, H. Lou, J. Ye, W. Bai, L. Wang, L. Li, W. Wu, Z. Xu, G. Wang, Z. Zhang, L. Zhang, Preparation and energy storage performance of transparent dielectric films with two-dimensional platelets, *Composites Science and Technology*, 2019, **182**, 107759, doi: 10.1016/j.compscitech.2019.107759.

[37] R. Zhang, Q. Sheng, L. Ye, S. Long, B. Zhou, F. Wen, J. Yang, G. Wang, W. Bai, Two-dimensional $SrTiO_3$ platelets induced the improvement of energy storage performance in polymer composite films at low electric fields, *Ceramics International*, 2022, **48**, 7145-7152, doi: 10.1016/j.ceramint.2021.11.274.

[38] Z. Pan, B. Liu, J. Zhai, L. Yao, K. Yang, B. Shen, $NaNbO_3$ two-dimensional platelets induced highly energy storage density in trilayered architecture composites, *Nano Energy*, 2017, **40**, 587-595, doi: 10.1016/j.nanoen.2017.09.004.

[39] Z. Pan, Q. Ding, L. Yao, S. Huang, S. Xing, J. Liu, J. Chen, J. Zhai, Simultaneously enhanced discharge energy density and efficiency in nanocomposite film capacitors utilizing two-dimensional $NaNbO_3$@Al_2O_3 platelets, *Nanoscale*, 2019, **11**, 10546-10554, doi: 10.1039/c9nr00874h.

[40] J. Chen, Z. Shen, Q. Kang, X. Qian, S. Li, P. Jiang, X. Huang, Chemical adsorption on 2D dielectric nanosheets for matrix free nanocomposites with ultrahigh electrical energy storage, *Science Bulletin*, 2022, **67**, 609-618, doi: 10.1016/j.scib.2021.10.011.

[41] Q. Li, K. Han, M. R. Gadinski, G. Zhang, Q. Wang, High energy and power density capacitors from solution-processed ternary ferroelectric polymer nanocomposites, *Advanced Materials*, 2014, **26**, 6244-6249, doi: 10.1002/adma.201402106.

[42] L. Li, J. Dong, R. Hu, X. Chen, Y. Niu, H. Wang, Wide-bandgap fluorides/polyimide composites with enhanced energy storage properties at high temperatures, *Chemical Engineering Journal*, 2022, **435**, 135059, doi: 10.1016/j.cej.2022.135059.

[43] D. Ai, H. Li, Y. Zhou, L. Ren, Z. Han, B. Yao, W. Zhou, L. Zhao, J. Xu, Q. Wang, Tuning nanofillers in *in situ* prepared

polyimide nanocomposites for high-temperature capacitive energy storage, *Advanced Energy Materials*, 2020, **10**, 1903881, doi: 10.1002/aenm.201903881.

[44] P. Hu, W. Sun, M. Fan, J. Qian, J. Jiang, Z. Dan, Y. Lin, C.-W. Nan, M. Li, Y. Shen, Large energy density at high-temperature and excellent thermal stability in polyimide nanocomposite contained with small loading of $BaTiO_3$ nanofibers, *Applied Surface Science*, 2018, **458**, 743-750, doi: 10.1016/j.apsusc.2018.07.128.

[45] M. Feng, Y. Feng, C. Zhang, T. Zhang, X. Tong, Q. Gao, Q. Chen, Q. Chi, Enhanced high-temperature energy storage performance of all-organic composite dielectric *via* constructing fiber-reinforced structure, *Energy & Environmental Materials*, 2024, **7**, e12571, doi: 10.1002/eem2.12571.

[46] X. Li, H. Luo, C. Yang, F. Wang, X. Jiang, R. Guo, D. Zhang, Enhancing high-temperature energy storage performance of PEI-based dielectrics by incorporating ZIF-67 with a narrow bandgap, *ACS Applied Materials & Interfaces*, 2023, **15**, 41828-41838, doi: 10.1021/acsami.3c06778.

[47] H. Li, L. Ren, D. Ai, Z. Han, Y. Liu, B. Yao, Q. Wang, Ternary polymer nanocomposites with concurrently enhanced dielectric constant and breakdown strength for high-temperature electrostatic capacitors, *InfoMat*, 2020, **2**, 389-400, doi: 10.1002/inf2.12043.

[48] J. Zhi, J. Wang, Z. Shen, B. Li, X. Zhang, C.-W. Nan, Nanofiber-reinforced polymer nanocomposite with hierarchical interfaces for high-temperature dielectric energy storage applications, *Science China Materials*, 2023, **66**, 2652-2661, doi: 10.1007/s40843-022-2412-2.

[49] J. Li, X. Liu, Y. Feng, D. Chen, Y. Li, D. Yue, B. Huang, J. Yin, Constructing bidirectional-matched interface between polymer and 2D nanosheets for enhancing energy storage performance of the composites, *Energy Storage Materials*, 2023, **54**, 605-614, doi: 10.1016/j.ensm.2022.11.009.

[50] Q. Li, L. Chen, M. R. Gadinski, S. Zhang, G. Zhang, H. U. Li, E. Iagodkine, A. Haque, L.-Q. Chen, T. N. Jackson, Q. Wang, Flexible high-temperature dielectric materials from polymer nanocomposites, *Nature*, 2015, **523**, 576-579, doi: 10.1038/nature14647.

[51] Q.-K. Feng, D.-F. Liu, Y.-X. Zhang, J.-Y. Pei, S.-L. Zhong, H.-Y. Hu, X.-J. Wang, Z.-M. Dang, Significantly improved high-temperature charge-discharge efficiency of all-organic polyimide composites by suppressing space charges, *Nano Energy*, 2022, **99**, 107410, doi: 10.1016/j.nanoen.2022.107410.

[52] W. Sun, X. Lu, J. Jiang, X. Zhang, P. Hu, M. Li, Y. Lin, C.-W. Nan, Y. Shen, Dielectric and energy storage performances of polyimide/$BaTiO_3$ nanocomposites at elevated temperatures, *Journal of Applied Physics*, 2017, **121**, 244101, doi: 10.1063/1.4989973.

[53] S. Luo, J. Yu, T. Q. Ansari, S. Yu, P. Xu, L. Cao, H. Huang, R. Sun, C.-P. Wong, Elaborately fabricated polytetrafluoroethylene film exhibiting superior high-temperature energy storage performance, *Applied Materials Today*, 2020, **21**, 100882, doi: 10.1016/j.apmt.2020.100882.

[54] Q. Zhang, X. Chen, B. Zhang, T. Zhang, W. Lu, Z. Chen, Z. Liu, S. H. Kim, B. Donovan, R. J. Warzoha, E. D. Gomez, J. Bernholc, Q. M. Zhang, High-temperature polymers with record-high breakdown strength enabled by rationally designed chain-packing behavior in blends, *Matter*, 2021, **4**, 2448-2459, doi: 10.1016/j.matt.2021.04.026.

[55] C. Yuan, Y. Zhou, Y. Zhu, J. Liang, S. Wang, S. Peng, Y. Li, S. Cheng, M. Yang, J. Hu, B. Zhang, R. Zeng, J. He, Q. Li, Polymer/molecular semiconductor all-organic composites for high-temperature dielectric energy storage, *Nature Communications*, 2020, **11**, 3919, doi: 10.1038/s41467-020-17760-x.

[56] H. Li, D. Ai, L. Ren, B. Yao, Z. Han, Z. Shen, J. Wang, L.-Q. Chen, Q. Wang, Scalable polymer nanocomposites with record high-temperature capacitive performance enabled by rationally designed nanostructured inorganic fillers, *Advanced Materials*, 2019, **31**, e1900875, doi: 10.1002/adma.201900875.

[57] Z. Wu, H. Zhou, Q. Guo, Z. Liu, L. Gong, Q. Zhang, G. Zhong, Z. Li, Y. Chen, Enhanced dielectric properties in polyimide nanocomposites containing barium titanate@ polydopamine core-shell nanoparticles, *Journal of Alloys and Compounds*, 2020, **845**, 156171, doi: 10.1016/j.jallcom.2020.156171.

Open Access